Testing the topological insulator behavior of half-Heusler PdYBi and PtYBi (111) epitaxial thin films

V. Palin [1,2] A. Anadón [1] S. Andrieu [1,*] Y. Fagot-Revurat,[1] C. de Melo [1,†] J. Ghanbaja,[1] O. Kurnosikov [1]
S. Petit-Watelot [1] F. Bertran [2] and J.-C. Rojas-Sánchez [1]

[1]*Institut Jean Lamour, Université de Lorraine / CNRS, UMR7198, 54011 Nancy, France*
[2]*Synchrotron SOLEIL, L'Orme des Merisiers, Départementale 128, F-91190 Saint-Aubin, France*

Topological insulators are promising materials in condensed-matter physics on the grounds that they host a peculiar spin texture that can generate very high spin-to-charge current interconversion, significantly relevant for up-and-coming low-energy-consumption spintronics devices. The goal of this study is to explore a promising family of topological materials showing distinctive properties such as high tunability—the half-Heuslers. We focus on the epitaxial growth of PdYBi and PtYBi thin films, which were grown and characterized on a series of interconnected UHV setups, allowing us to get a full set of *in situ* surface characterizations, such as electron diffraction, scanning tunneling microscopy, and angle-resoled photoemission spectroscopy. *Ex situ* structural characterization using standard x-ray diffraction and scanning transmission electron microscopy were used to control the crystalline quality and chemical ordering in the thin films. Angle-resolved photoemission spectroscopy was performed and reveals the presence of linear states around the Γ point of the Brillouin zone. Furthermore, we carry out thermospin transport measurements using on-chip devices with a designed geometry for a controlled heat propagation to test the potential interconversion efficiency of our compounds, finding a larger value of the spin Seebeck coefficient than that of platinum for different thicknesses for both PdYBi and PtYBi. This observation opens a pathway to develop efficient spin interconversion materials using half-Heuslers.

I. INTRODUCTION

Spintronics relies on the exploitation of the intrinsic spin of the electron and its magnetic moment, allowing the design of new kinds of magnetic storage. The birth of spintronics took place in 1988 when Albert Fert and Peter Grünberg discovered simultaneously the giant magnetoresistance (GMR) effect [1,2]. This effect has led to the development of numerous sensors, especially hard drive disk's read heads. More recently, spin transfer torque–based [3] magnetic random access memory (STT-MRAM) has been used as a nonvolatile memory to store data and are already implemented in some commercial applications [4,5]. One of the main drawbacks of STT-MRAMs is the high current needed to write. This can cause a loss of reliability due to damage in the tunneling barrier, and further research is needed to overcome this issue. In this sense, the recent field of spin orbitronics can provide some tools to obtain more reliable devices by making use of the electron spin to generate pure spin currents in materials with spin-orbit coupling (SOC) that can be used to switch the magnetization of an adjacent magnetic layer [6]. These spin currents can be generated by two different effects, namely, the spin Hall effect [7] in the bulk of the material and the Edelstein effect [8] that occurs at the surfaces or interfaces.

The materials with SOC typically used for spin-orbitronics devices are heavy metals (HMs), where significant spin-to-charge current (S2C) interconversion has been reported (W [9], Pt [9], or Ta [10]). One of the main challenges of spin orbitronics is to get interconversion between charge current and spin current with the highest efficiency. Recently, it has been proposed to replace such HM by topological insulators (TIs) [11], which are thought to provide a more efficient spin-to-charge interconversion and thus to reduce the magnetization's switching current [12]. Since their discovery, TIs have attracted interest due to their topologically protected spin texture. The surface state of a 3D-TI consists of a Dirac cone in which the spin is locked to the momentum. This property, named spin-momentum locking [13], avoids backscattering and leads to very high S2C interconversion. Due to this property, TIs are perfect candidates to generate huge torques on an adjacent FM, allowing it to switch its magnetization. The most thoroughly studied TIs are the Bi-based binary compounds such as Bi_2Se_3 [14], Bi_2Te_3 [15], or BiSb, where topological surface states (TSSs) were identified [16] and large S2C interconversions were achieved [17,18].

Some Heusler alloys were predicted to host a nontrivial nature in 2010 [19]. They come from the half-Heusler family with an XYZ formula unit (Fig. 1). By considering SOC in band structure calculations, it was shown that a band inversion can occur at the Γ point of the Brillouin zone (BZ). Similarly to what happens in HgTe [20], the Γ_8 and Γ_6 bands are inverted, leading to a nontrivial topology where TSS should appear. Some interesting results have already been obtained on rare-earth platinum bismuth Heusler alloys [21–23], but the
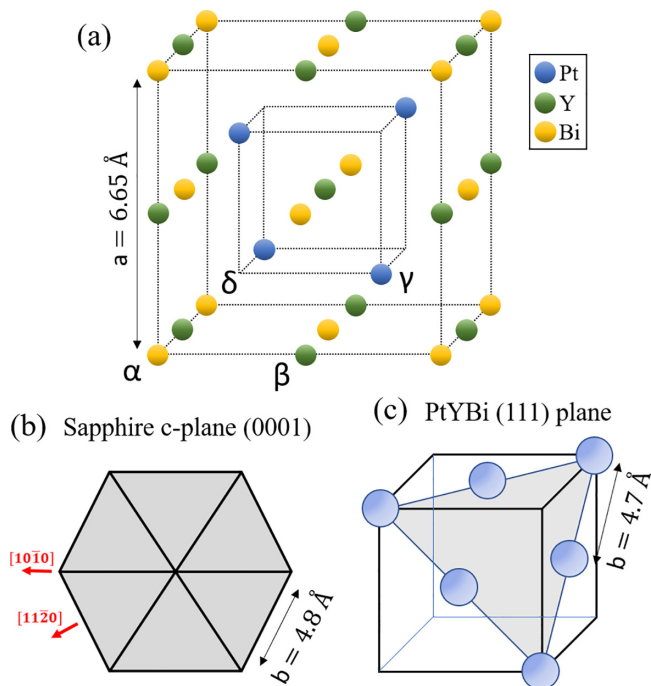
FIG. 1. (a) C1$_b$ structure of PtYBi. Note that in half-Heusler compound α, β and γ are occupied although δ is not. (b), (c) Epitaxial relationship between (0001) sapphire plane and (111) PtYBi plane. This is the same for PdYBi ($a = 6.63$ Å).

observation and presence of TSS is still under debate. Moreover, most of these studies were performed in bulk materials and suffer from a lack of thin-film growth that would allow fine-tuning of cell parameters. This work is thus dedicated to the study of half-Heusler thin films predicted to be TI. Several candidates were proposed by Chadov *et al.* [19] and Lin *et al.* [24], leading to 50 Heusler alloys possessing a band inversion similar to that of HgTe. Here we focused on PtYBi and PdYBi. Concerning PtYBi, a band inversion is predicted thus classified as a nontrivial TI [19]. This TI behavior was actually observed in bulk PtYBi comparing angle-resolved photoemission spectroscopy (ARPES) and band structure calculations [23]. The situation is not so clear concerning PdYBi. On the one hand, PdYBi was first predicted to be a topologically trivial Heusler alloy with a positive Γ_6 and Γ_8 bands difference that is very close to zero [19]. It was also shown theoretically to be at the limit of inversion according to its lattice spacing [25]. On the other hand, a band inversion was recently predicted in this material by using *ab initio* calculations considering a hydrostatic pressure to vary the lattice spacing [26]. They obtained a PdYBi nontrivial behavior in a large range of lattice spacing. Finally, the band inversion can be obtained when growing these materials in thin films where strain often occurs, as shown in PtLuBi [27] and in PdYBi [19,26]. To summarize, the nontriviality in PdYBi thin films is still an open question.

The goal of this study is to prepare PdYBi and PtYBi epitaxial thin films and explore their topological nature. Thin-film growth was performed by molecular beam epitaxy (MBE) with a particular attention paid to crystalline growth, stoichiometry, and atomic disorder that can strongly affect the

band structure and the electronic properties. Reflection high-energy electron diffraction (RHEED) and scanning tunneling microscopy (STM) were used to check the epitaxial process. The films' structure was determined by x-ray diffraction (XRD). Scanning transmission electron microscopy (STEM) was used to check the epitaxy and chemical ordering by using the high-angle annular dark field mode (HAADF). ARPES studies were conducted to map the band structure of the films. Finally, we performed thermospin transport measurements on on-chip devices with controlled geometry of the heat flux to investigate the efficiency of S2C interconversion in half-Heusler alloys in comparison to conventional HMs, namely, Pt.

II. SAMPLE PREPARATION AND STRUCTURAL CHARACTERIZATION

A. Experimental growth details

All the samples were grown at the Institut Jean Lamour in a special MBE chamber dedicated to the growth of metallic alloys. In this so-called quaternary MBE, 24 elements are available using three electron guns with six pockets each and six Knudsen cells [28]. This wide variety of elements easily allows ternary or quaternary Heusler compounds to be formed on numerous buffer layers. This chamber is connected to a 70-m UHV tube facility at the Institut Jean Lamour. Therefore characterization experiments such as x-ray and Auger electron spectroscopy, STM, and ARPES can be performed without breaking the vacuum. The growth process consisted in coevaporating the three elements at the same time under a base pressure equal to 3.10^{-11} Torr in the MBE. Bi was evaporated from a Knudsen cell, while Y, Pt, and Pd were evaporated from e-gun evaporation sources. To get the 1:1:1 stoichiometry, fluxes were fixed to $\Phi_{Pd/Pt} = \Phi_Y = \Phi_{Bi} = 5 \times 10^{13}$ at cm^{-2} s^{-1}. The flux control was possible by measuring the growth rate using quartz microbalances (QMs), owing to the link between flux and growth rate by the following formula:

$$\Phi_i = v_i n_i = v_i \frac{\rho_i N_{Av}}{M_i}, \tag{1}$$

with n_i the volume density, ρ_i the mass density, N_{Av} the Avogadro number, M_i the molar mass, and v_i the growth rate. For instance, using PdYBi density (9.25 g cm^{-3}), the growth rates of Pd, Y, and Bi were regulated to the target rates 0.0950, 0.0794, and 0.187 Å s^{-1}, respectively. This corresponds to a total alloy growth rate of 0.36 Å s^{-1}. The Pd, Pt, and Y fluxes using e-guns were fixed by regulating the growth rates in real time using dedicated QMs. The Bi flux was fixed by adjusting the cell temperature to get the proper growth rate using a QM located at the sample's place. This process leads us to control the stoichiometry with an accuracy on each element better than 1% (see [28] for more details). In addition, the epitaxial growth was followed in real time thanks to a RHEED setup coupled to the MBE. The substrate can be heated during the growth, and the temperature is measured by using a pyrometer focused on the sample surface (denoted by T$_{pyro}$ hereafter). Since the emissivity of both PdYBi and PtYBi are not known, we fixed it arbitrarily to 0.85. Finally, both PdYBi and PtYBi films were grown on sapphire substrates (0001) oriented. A
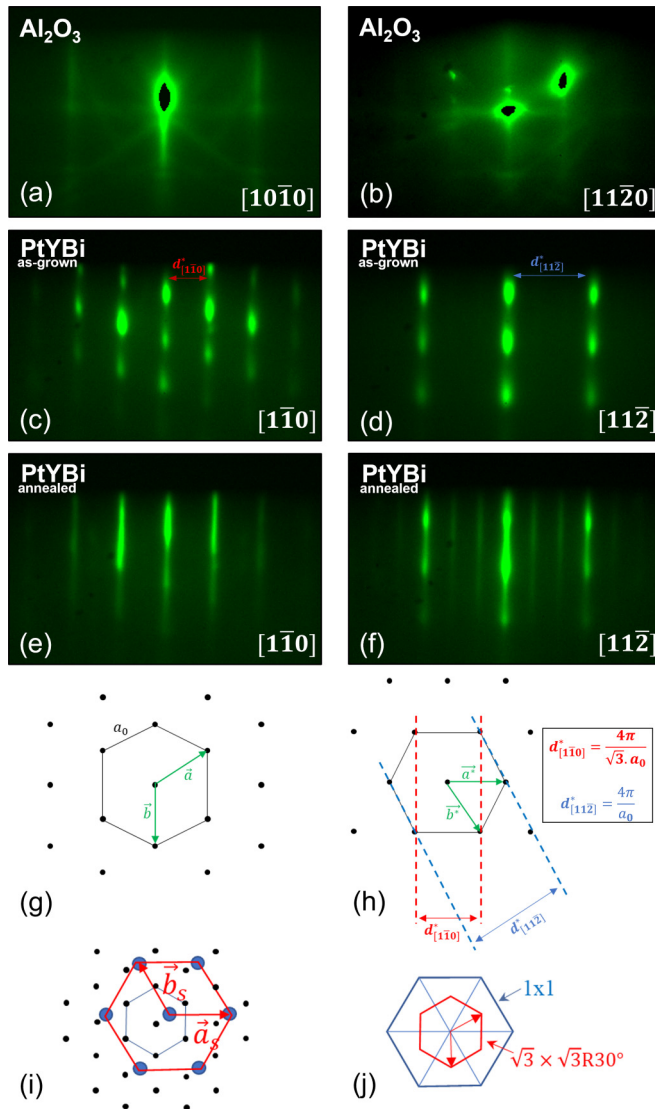
FIG. 2. (a), (b) RHEED patterns of c-plane Al_2O_3 substrate along $[11\bar{2}0]$ and $[10\bar{1}0]$ azimuths. RHEED patterns along the $[10\bar{1}0]$ and $[11\bar{2}0]$ azimuths for as-grown PtYBi sample [(c) and (d)] and after annealing [(e) and (f)], showing a $\sqrt{3}\times\sqrt{3}$ R30° reconstruction leading to $\frac{1}{3}$ and $\frac{2}{3}$ supplementary streaks along the $[11\bar{2}]$ azimuth. (g) PtYBi (111) surface lattice and (h) corresponding 1×1 reciprocal lattice. (i) $\sqrt{3}\times\sqrt{3}$ R30° surface reconstruction and (j) corresponding reciprocal lattice compared to the 1×1 of (h).

growth along the (111) direction is expected as sketched in Fig. 1.

B. Structural and electronic properties of PtYBi thin films

The growth of PtYBi was done on top of sapphire with a deposition temperature of $T_{pyro} = 540\,°C$. A Wolmer-Weber growth process was observed: three-dimensional (3D) islands grow separately at first and coalesce after a few nanometers of deposition. The RHEED patterns obtained after a 20-nm-thick film growth are shown in Figs. 2(c) and 2(d). The RHEED streaks are spotty, indicating that the films are rough due to the 3D growth. An increase of the surface quality was achieved by annealing the sample up to $T_{pyro} \approx 630\,°C$, but the streaks
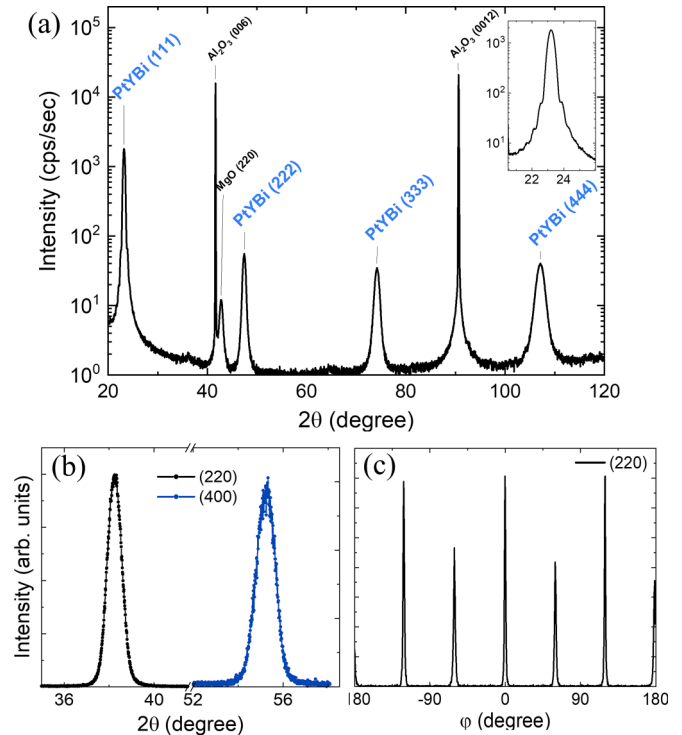

FIG. 3. (a) Typical $\theta/2\theta$ XRD scan for PtYBi. The inset on the upper part is a zoom of the PtYBi (111) peak showing the presence of Kiessig fringes. (b) Nonsymmetrical scans of the PtYBi sample allowing measurement of the (220) and (004) diffraction peaks (c) periodicity of (220) peak around the (111) growth direction showing a $\frac{\pi}{3}$ periodicity not expected in a cubic cell.

remained slightly spotty, indicating some remaining roughness. We tested higher annealing temperatures to smooth the surface, but Bi desorption thus occurs, which is detrimental for the stoichiometry. Nonetheless, reconstructions along the $[11\bar{2}]$ azimuth are visible, indicating the presence of terraces. The surface probably consists of 3D islands with flat terraces on their top, as will be confirmed by transmission electron microscopy (TEM). The appearance of new $\frac{1}{3}$ and $\frac{2}{3}$ streaks on RHEED patterns along the $[11\bar{2}]$ azimuth [Fig. 2(f)] corresponds to a $\sqrt{3}\times\sqrt{3}$ R30° surface reconstruction as explained in Figs. 2(i) and 2(j). Finally, the in-plane lattice spacing extracted from the RHEED patterns is equal to 0.47 nm, in agreement with the (110) PtYBi bulk distance.

As RHEED analysis only gives information on the surface lattice, XRD was used to determine the layer crystalline structure and its lattice parameters. Two setups were used: symmetrical and nonsymmetrical configurations. All these measurements were carried out with $\lambda = 1.540\,56\,Å$. The configuration symmetric to the sample surface uses the $\theta/2\theta$ mode. A typical $\theta/2\theta$ XRD pattern of a 20-nm-thick PtYBi film grown on sapphire and capped with 20 nm of MgO is given in Fig. 3(a). In addition to sapphire and MgO diffraction peaks, several peaks coming from the PtYBi(111) family are observed, confirming this growth axis as previously revealed by RHEED patterns. No parasite peak is observed, showing a perfect single-crystalline growth. Moreover, PtYBi peaks are sharp, and the inset on the upper part of Fig. 3(a) shows a
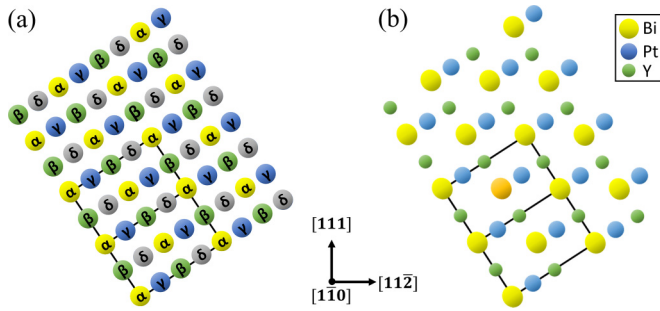
FIG. 4. (a) $[1\bar{1}0]$ zone axis atomic columns for Heusler structure indicating the α, β, γ, and δ site position of Fig. 1. (b) Expected atomic column arrangement of $[1\bar{1}0]$ PtYBi zone axis where Bi, Pt, and Y go, respectively, on α, β, and γ sites. δ sites are empty since they are not filled in the case of the ordered half-Heusler structure. The sizes of the circles are a relative representation of the expected intensities.

zoom of the (111) peak of PtYBi, unveiling the presence of Kiessig fringes as another proof of good thin-film crystallinity. By assuming the PtYBi unit cell to be perfectly cubic (i.e., $a = b = c$), the cell parameter can be extracted thanks to Bragg's law, which gives $a = 6.64$ Å, in perfect agreement with the expected C1$_b$ half-Heusler structure [Fig. 1(a)]. The nonsymmetrical configuration allows us to obtain nonspecular peaks, such as (004) and (220), shown in Fig. 3(b). The cell parameter extracted from the (004) and (220) peaks is 6.65 Å, similar to that of peak (111). Finally, a $\frac{2\pi}{3}$ periodicity around the (111) direction is expected for the C1$_b$ structure. We thus recorded the different (220) peaks turning around this direction [Fig. 3(c)], but a $\frac{\pi}{3}$ periodicity was observed. This is a strong indication of the presence of two domains turned by 180°, as will be confirmed by TEM in the following.

The crystalline quality and chemical ordering of the films were thus studied using STEM. Cross sections were prepared using focused-ion-beam etching with Ga ions. We chose the $[1\bar{1}0]$ zone axis of the C1$_b$ structure, resulting in the pattern represented in Fig. 4(b). This [110] zone axis is very suitable to study chemical disorder in these compounds, since it presents only monoelemental columns if the chemical ordering is perfect. In particular, this expected pattern has empty columns due to the vacancies present in the δ site of the half-Heusler structure [see Fig. 1(a)].

TEM measurements were done on a JEM-ARM 200F Cold FEG microscope operating with a 200-kV acceleration voltage. Two operating modes were used, namely, TEM (bulk structure) and STEM-HAADF (low-magnification images with atomic contrast). The achievable resolution on the microscope is 1.2 Å in TEM mode, while STEM mode can go down to 0.78 Å. A STEM image of PtYBi is given in Fig. 5(a). A Fe/Al capping layer was used here, and a Pt layer was grown on the whole stack for cross-section preparation. The epitaxial growth along (111) is confirmed, but the surface is rough, as expected from RHEED analysis. In fact, this film shape results from the coalescence between two 3D islands. The top of the islands are flat, corresponding to (111) terraces (which is expected since this corresponds to the smallest surface energy in such an fcc-like structure). Such layer shape perfectly explains the observed RHEED patterns
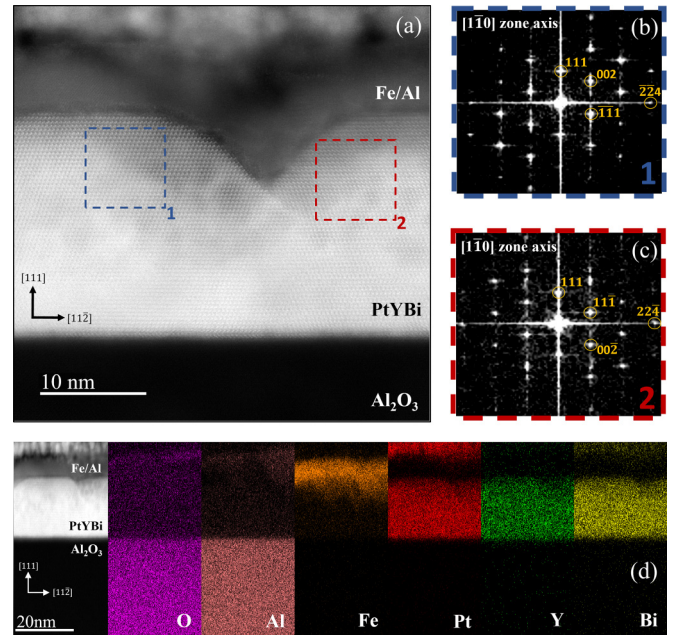

FIG. 5. (a) STEM image of Al$_2$O$_3$/PtYBi/Fe/Al sample. Fe/Al is the capping layer and Pt is deposited for cross-section preparation. (b), (c) FFT corresponding to both islands, unveiling the presence of two domains turned by 180°. (d) STEM EDX maps of different elements along the cross section, indicating no mixing and homogeneous Pt, Y, and Bi concentrations.

(streaks coming from flat surfaces and spots due to the roughness). In addition, one can see that these two different islands are not oriented in the same way. They are both C1$_b$ but are turned by 180°, as confirmed by Fourier transform on frames taken in each island [labeled 1 and 2 in Figs. 5(b) and 5(c)]. The diffraction patterns are asymmetric, which allows us to distinguish the two different domains lying in the sample. One should note that this resulting layer structure in domains does not come from any composition variation along the layer. Indeed, energy-dispersive x-ray (EDX) spectroscopy performed on TEM cross sections [Fig. 5(d)] shows no mixing between the different layers and homogeneous Pt, Y, and Bi concentrations in the half-Heusler layer.

In order to distinguish clearly the atomic columns, images with higher magnification were collected. High-magnification HAADF-STEM processed images are given in Figs. 6(a) and 6(b) for both identified areas of Fig. 5(a) and make possible a comparison with the expected pattern. The chemical ordering was checked in each domain of Fig. 5(a), and the results are shown in Fig. 6. The heavier elements appear brighter while the lighter ones are darker. Thus it is easy to identify Bi, Pt, and Y columns since the intensity is linked to the number of electrons: Bi ($Z = 83\,e^-$) is the brightest element, and then comes Pt ($Z = 78\,e^-$) and Y ($Z = 39\,e^-$). For each domain, the observed atomic column arrangement fits perfectly with the expected ones [see Fig. 4(b)], assuming no chemical disordering. Even if the pattern is clearly visible, intensity line profiles are performed and the agreement with the ideal atomic arrangement is perfect. Moreover, the presence of both domains clearly explained the $\frac{\pi}{3}$ periodicity around the (111) peaks observed by XRD.
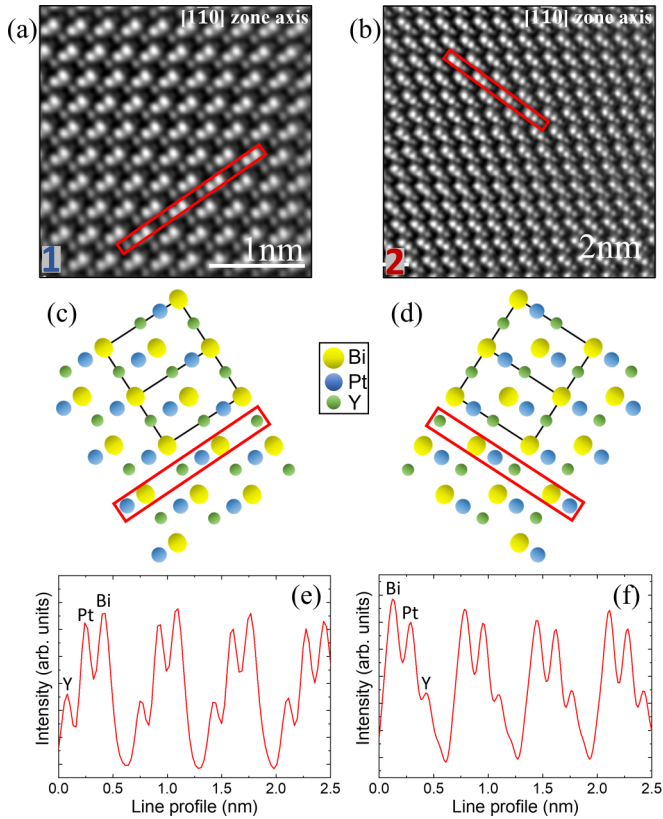
FIG. 6. (a),(c),(e) and (b),(d),(f) are respectively the treated STEM-HAADF images, the predicted patterns, and the line profiles for the two domains labeled 1 and 2 and identified in Fig. 5(a).

FIG. 7. (a) PtYBi LEED pattern at 50-eV electron energy depicting the 1×1 hexagonal lattice (brown dashed line). The first Brillouin zone is represented in the plain yellow line. Note that it corresponds to the $\sqrt{3} \times \sqrt{3}$ R30° surface reconstruction, but the ARPES measurements are not sensitive to it. The white dashed line represents the slit of the ARPES analyzer. (b) Constant energy contour map at $E_B = -300$ meV, where the first Brillouin zone is given in the plain yellow line. (c) Band mapping along $\overline{\Gamma M}$ showing bands with linear dispersion around $\overline{\Gamma}$. The TSS shown in red is identified with [23].

The electronic band structure was probed using the ARPES setup connected to the Daum UHV tube at Institut Jean Lamour. The samples were thus grown in the MBE chamber just before the ARPES experiments. They were first oriented using a low-energy electron diffraction (LEED) setup connected to the ARPES chamber [Fig. 7(a)]. The LEED images were formed by the 1×1 unit cell together with the $\sqrt{3} \times \sqrt{3}$ R30° surface reconstruction observed by RHEED, but with smaller intensities. At this stage one thus has to be very careful regarding the ARPES measurements, because the first BZ corresponding to the 1×1 unit cell coincides with the surface reconstruction. A typical constant energy contour map at a binding energy $E_B = -300$ meV is shown in Fig. 7(b). It should be noted that a sixfold symmetry is observed instead of a threefold one expected along the (111) axis in such a CFC-like half-Heusler structure, simply due to the presence of the two domains rotated by 180°. The band mapping allows us to identify the hexagonal shape of the first BZ. Numerous Fermi pockets already labeled in literature [23,29] can be discerned around the $\overline{K}$ points. They also linked the spectral weight around the $\overline{\Gamma}$ point as twin hexagonal pockets that cannot be clearly identified here since the obtained resolution seems to depict a circular shape. A second $\overline{\Gamma}$ point is visible in the constant energy contour, and an estimation of the distance between two $\overline{\Gamma}$ points is possible. The extracted value of $k_{//} = 1.54$ Å^{-1} is in perfect agreement with the expected value for the PtYBi first BZ. Finally, no additional state due to surface reconstructions is noticed, since very similar ARPES band
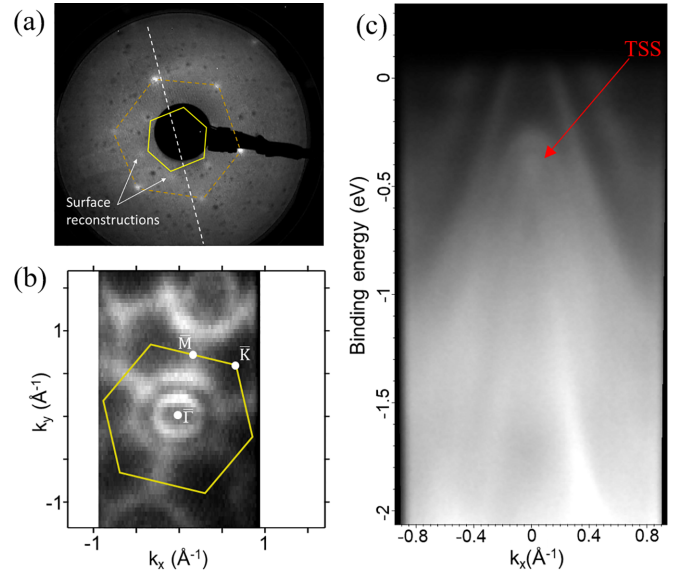
structures were observed in the cleaved bulk sample [23,29]. Indeed, in light of this constant energy mapping, it seems that the $\sqrt{3} \times \sqrt{3}$ R30° surface reconstruction did not impact the band structure in our experimental conditions. This is not so surprising, since surface reconstructions are not always visible in ARPES measurements. Finally, band mapping of Fig. 7(c) unveils multiple bands crossing the Fermi energy, where some of them show a linear dispersion around the $\overline{\Gamma}$ point. According to the literature, these linear states crossing the Fermi energy are trivial surface states, and their nature has nothing to do with topology. Nonetheless, an additional X-shape band dispersing is present and lies in the bulk bands at a binding energy of around $E_B = -0.45$ eV. Band-structure calculations performed in literature [23,29] labeled this crossing point at $\overline{\Gamma}$ as a TSS manifesting the nontrivial topology of PtYBi. However, the situation may be more complex in a real system (thin films, interfaces, strain, roughness, etc.), so our strategy was to test some topological behavior by using spin-charge conversion in transport measurement.

C. Structural and electronic properties of PdYBi thin films

PdYBi thin films were prepared and studied with the same global method. The growth was performed at a lower temperature ($T_{pyro} = 360$ °C) since Pd is more mobile on the surface than Pt. The growth process is Stranski-Krastanov, also known as layer-plus-island growth as shown by RHEED patterns. At the beginning, the film exhibits a 2D surface after a few seconds with nice homogeneous RHEED streaks
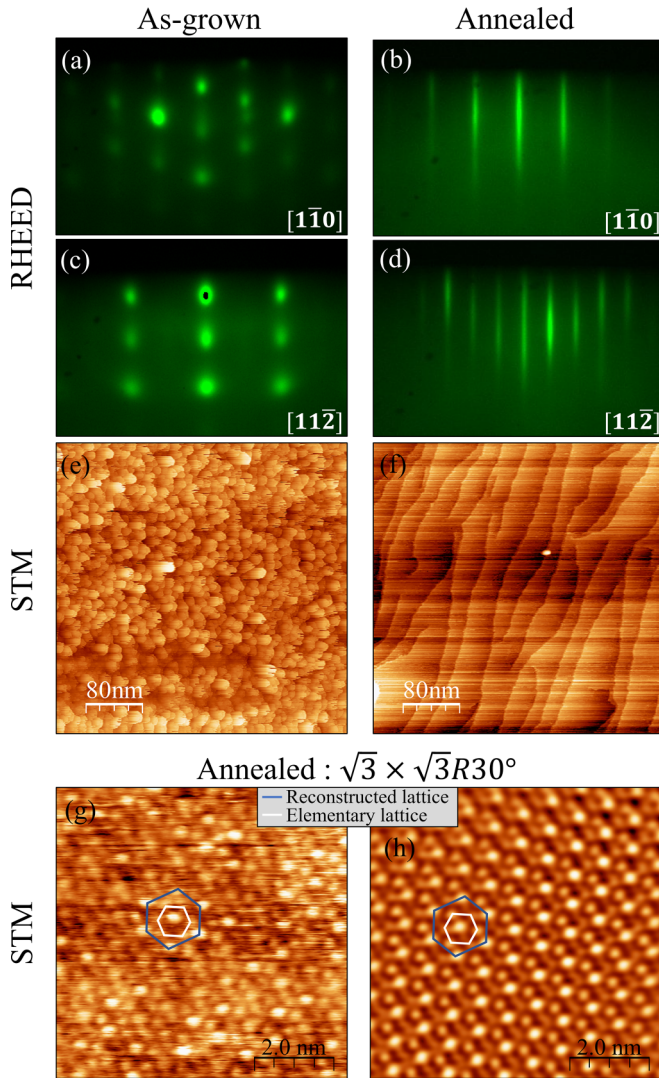
FIG. 8. As-grown (a), (c) and after annealing (b), (d) PdYBi RHEED patterns. STM images obtained on as-grown (e) and after annealing (f) PdYBi film. Raw (g) and processed (h) STM images with atomic resolution obtained on annealed films confirming the $\sqrt{3} \times \sqrt{3}R30°$ surface reconstruction deduced from RHEED.
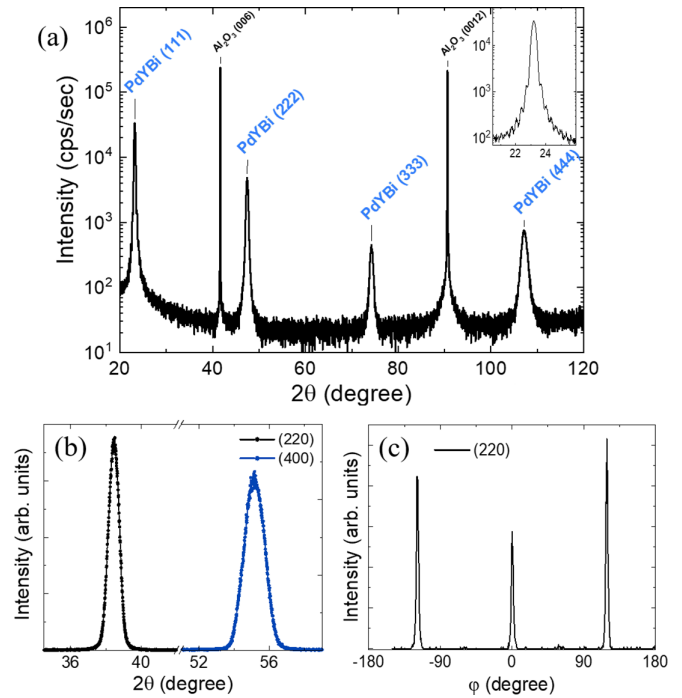

FIG. 9. PdYBi thin-film XRD analysis similar to Fig. 3. (a) $\theta/2\theta$ XRD scan, (b) (220) and (004) diffraction peaks, and (c) $\frac{2\pi}{3}$ periodicity of (220) peaks around (111). Note that this periodicity differs from PtYBi.

due to a layer-by-layer-like growth. After a critical thickness around 1 nm, spotty RHEED streaks appeared, meaning that a 3D growth process started [Figs. 8(a), 8(c), and 8(e)]. Here again the in-plane lattice spacing extracted from the RHEED patterns is equal to 0.47 nm. An increase of the surface quality was achieved by annealing the sample up to $T_{pyro} \approx 550°C$, leading to smooth surfaces [Figs. 8(b), 8(d), and 8(f)]. Attention must be paid to the annealing process, since higher substrates temperatures can lead to dewetting. This annealing also lead to a $\sqrt{3} \times \sqrt{3}R30°$ surface reconstruction as for PtYBi. This growth process was confirmed by using STM [Figs. 8(g) and 8(h)]. Large-scale STM images on as-grown films actually shows rough surfaces with islands, whereas very smooth surfaces with long terraces were observed after annealing. The atomic resolution obtained on annealed (smooth) samples confirms the $\sqrt{3} \times \sqrt{3}R30°$ surface reconstruction deduced from electron diffraction.

The XRD analysis done on PdYBi leads to results very similar to PtYBi, except for the symmetry rotation around the (111) axis [Fig. 9(c)]. The epitaxy along (111) is confirmed by the $\theta/2\theta$ XRD diagram, and the extracted lattice distances from (111), (004), and (220) are similar within the error bars (i.e., 6.63 Å, 6.65 Å, and 6.62 Å, respectively). Finally, the (220) peak periodicity around the (111) direction was also checked. Contrary to PtYBi, the expected $\frac{2\pi}{3}$ periodicity is observed, meaning that a unique domain is now obtained.

The TEM/STEM-HAADF analysis of PdYBi films is summarized in Figs. 10 and 11. MgO was used as a capping layer to avoid contaminations and oxidation. The PdYBi surface is flat with low roughness as observed in RHEED. Again, the diffraction patterns confirm the (111) growth on sapphire and the [1$\bar{1}$0] zone axis. Moreover, the deposited PdYBi's thickness can be measured as 20.8 nm, in good agreement with the aimed 20 nm. EDX spectroscopy of the cross sections shows sharp interfaces without mixing and homogeneous Pd, Y, and Bi concentration in the half-Heusler layer.

The high-magnification HAADF-STEM image given in Fig. 11(a) highlights a noticeable difference with PtYBi films. In PdYBi films we did not observed two domains as in PtYBi, but another fundamental difference has to be noticed. The HAADF pattern in Fig. 11 does not fit the expected pattern of Fig. 4(b), as revealed by the intensity line profile. Indeed, due to the vacant site of half-Heusler structure, some columns should not be filled, but looking carefully at Fig. 11(a), no unfilled columns are observed. There are two possible ways to explain this column's filling. The first one is to consider several (small) domains in the cross section (and so in the sample) that are turned by 180° with respect to each other,
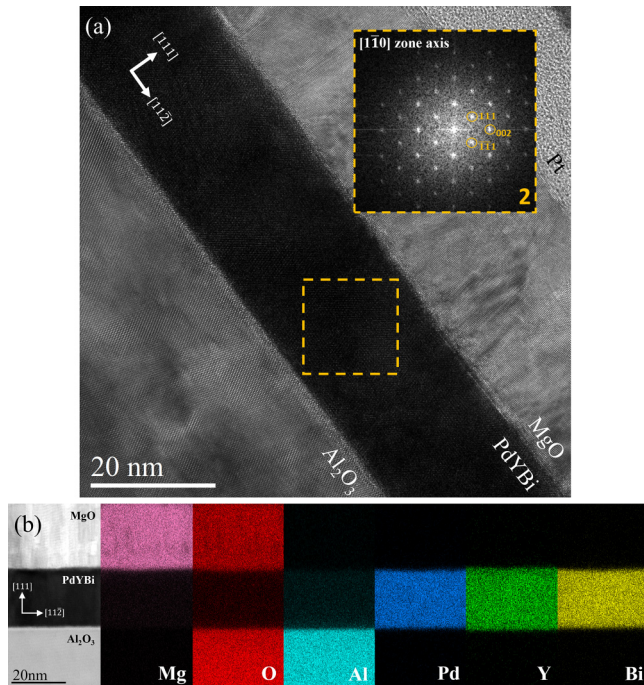
FIG. 10. (a) TEM image of Al_2O_3/PdYBi/MgO sample. MgO is the capping layer and Pt is deposited for cross-section preparation. The inset is a FFT of the yellow area checking the $[1\bar{1}0]$ zone axis. (b) STEM EDX map of different elements along the cross section indicating no mixing and homogeneous Pd, Y, and Bi concentrations.

but this is not consistent with the $\frac{2\pi}{3}$ periodicity of the (220) peaks observed by XRD. The second possibility is to consider chemical disorder in the unit cell. In the perfectly ordered structure Bi, Y, and Pd go respectively in the α, β, and γ positions, and the δ site is not occupied [Figs. 1(a) and 4(a)]. But Pd can swap between γ and δ sites. This leads to partially filled Pd columns that come to the same pattern observed in Fig. 11. Note that such a random distribution of Pd on γ and δ sites cannot lead to $\frac{\pi}{3}$ periodicity of (220) around (111), so the
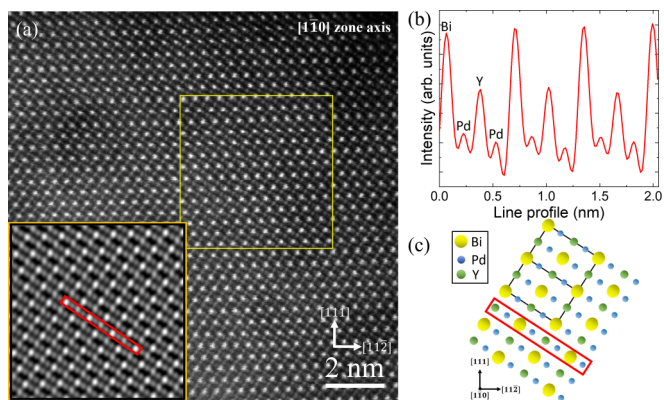

FIG. 11. (a) Raw STEM-HAADF image of PdYBi. The inset is a processed image of the yellow frame in the raw image. The better signal-to-noise ratio allows us to clearly distinguish the atomic columns and their intensities. (b) Intensity line profile performed on the inset red box area. (c) Sketch of the observed column pattern.
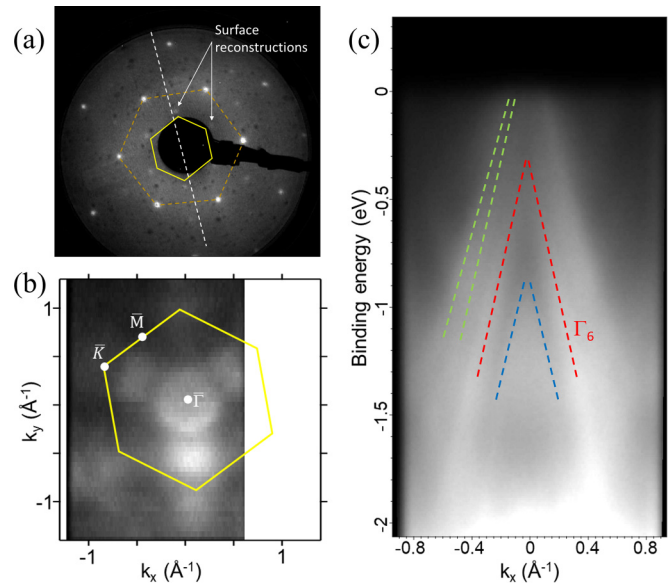

FIG. 12. (a) PdYBi LEED pattern at 50-eV electron energy depicting the 1×1 hexagonal lattice (brown dashed line). The first Brillouin zone is represented in the plain yellow line. The white dashed line represents the slit of the ARPES analyzer. (b) Constant energy contour map at $E_B = -500$ meV, where the first Brillouin zone determined by LEED is given by the plain yellow line. (c) Band mapping along $\overline{\Gamma K}$ showing bands with linear dispersion around the $\overline{\Gamma}$ point. Dashed lines are the calculated bands [26] which evidence the band inversion (Γ_6 bellow E_F).

$\frac{2\pi}{3}$ rotation symmetry in the cubic structure is conserved. This chemical disorder impacts the photoemission observations as shown hereafter.

The ARPES analysis is shown in Fig. 12. Again, the LEED images were formed by the 1×1 unit cell together with the $\sqrt{3} \times \sqrt{3}$ R30° surface reconstruction. A typical constant energy contour map at a binding energy $E_B = -500$ meV is shown in Fig. 12(b), where the calculated first BZ considering the 1×1 hexagonal lattice is indicated. Here a threefold symmetry is observed, contrary to the PtYBi energy contour map. This is not surprising since there are no domains in PdYBi. Electron pockets near $\overline{K}$ points can be identified since similar features have been observed in other Heusler compounds [21,23,29]. A ring at the center of the BZ $\overline{\Gamma}$ is visible and opened while increasing the binding energy. This is a typical signature of states with linear dispersion, but care must be taken since literature for other Heusler compounds labeled these states as trivial surface states. These bands with linear dispersion around the $\overline{\Gamma}$ point are unveiled in the band mapping given in Fig. 12(c). The multiple bands with linear dispersion may originate from Kramers pairs, since similar bands have been observed in other Heusler alloys [23]. It should be noted that the bands are not clearly defined. This cannot be due to some crystalline disorder, since RHEED, LEED, and XRD spectra show well-crystallized films and smooth 2D surfaces. We emphasize that it comes from the chemical disorder present in the lattice. One should note that this chemical disorder only affects the relative position of vacancies and Pd atoms in the half-Heusler structure. Thus a quite simple tight-binding modeling shows that the bands

stay the same considering this special disorder, whereas some band broadening is expected due to the irregular distribution of Pd and vacancies from one unit cell to the other. After these considerations, we can compare our results with the *ab initio* calculation proposed in Ref. [26]. These first-principles calculations allow us to clearly identify the bands on our ARPES measurements, as indicated by the dashed lines in Fig. 12(c). We clearly observe the Γ_6 band crossing around -0.3 eV, which is a clear indication that our PdYBi thin films have a nontrivial behavior.

III. THERMOSPIN TRANSPORT MEASUREMENTS

The band mapping of both compounds unveils a complex band structure where a straightforward TSS observation turns out to be complex. Multiple bands crossing the Fermi level are observed, with a TSS lying well below the Fermi energy according to previous works and theoretical calculations found in literature. Bands with linear dispersion cross the Fermi energy but may be due to trivial surface states. The nontrivial topological nature may lie in the additional crossing point observed below the Fermi energy since similar features have been published for other Heusler alloys. Fortunately, ARPES measurements are not the unique way to probe topological effects. The complex and unusual phenomena hosted by TIs can also manifest in transport measurements. In particular, thermospin measurements can help in evaluating the extent of the spin conversion in these materials and shed light on its origin, whether it is from TSS, bulk states, or a combination of both.

In this study the two half-Heuslers were characterized by thermospin measurements in order to assess the spin conversion. This spin conversion can be obtained from the strength of the spin Seebeck effect (SSE), which refers to the generation of a spin current J_S in magnetic materials as a result of a temperature gradient, ∇T. The SSE occurs due to thermally excited spin current in the FM owing to the gradient of temperature that can be driven by either magnons and/or spin-polarized charge carriers in conducting FM [30]. This thermally generated spin current $\mathbf{J}_S$ is parallel to the temperature gradient ∇T. When a HM (or a TI) layer is in direct contact with a FM layer under a temperature gradient, the generated spin current is injected in this adjacent layer and transformed into an electric voltage due to spin-orbit coupling. Indeed, the transverse spin current is converted into a longitudinal charge current by inverse spin Hall effect (ISHE) in the HM or inverse Edelstein effect (IEE) in the TI. A sketch of the SSE principle is given in Fig. 13. It can be summarized by the relation $\mathbf{E}_{ISHE} \propto \mathbf{J}_C \propto \mathbf{J}_S \times \boldsymbol{\sigma}$, with $\mathbf{J}_C$ the charge current created by ISHE (or IEE for the case of a TI) and detected along the x direction. $\mathbf{J}_S$ is the spatial direction of the thermally induced spin current which is perpendicular to the interface and parallel to ∇T (along the z direction). σ is the spin polarization and is parallel to the magnetization (along the y direction).

A series of samples dedicated to SSE measurements was prepared with the following stack: sapphire/half-Heusler (X nm)/MgO(barrier)/Fe(6 nm)/MgO(20 nm) with $X = 5$, 10, 20, and 30 nm. The MgO barrier was one monolayer thick (0.2 nm) for PdYBi and two monolayers thick for PtYBi
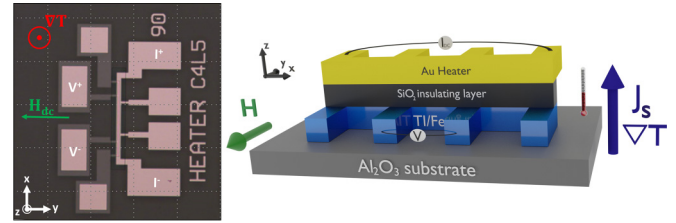

FIG. 13. On the left, spin Seebeck device image. On the right, sketch of the spin Seebeck device. A temperature gradient is applied along the z direction, thanks to the current injected in the Au heater, and generates a spin current J_S (along the z direction), which is in turns injected at the FM/TI interface. The thermally created spin current is converted by IEE (or ISHE for HM) in a longitudinal charge current (along the x direction) which is measured by a nanovoltmeter. The blue layer in the sketch represents the full sample stack detailed for each case in the text.

samples (rougher surface compared to PdYBi). MgO was used to protect the FM/TI interface, since TIs are sensitive to magnetic impurities due to their time-reversal symmetry (TRS)-breaking nature that can strongly affect the nontrivial topological phase and kill the TSS [13,31]. A 6-nm Fe ferromagnet was then deposited at room temperature. The samples were then covered by a 20-nm-thick MgO capping. In addition to these samples, a control and reference samples were fabricated. In the control sample the half-Heusler films are replaced by Pt in order to compare the spin-to-charge interconversion efficiency of PdYBi and PtYBi films with this well-known HM. The sample stack was thus sapphire/Pt(5 nm)/MgO(barrier)/Fe(6 nm)/MgO(20 nm). Finally, a Fe reference sample was deposited with the following stack: sapphire/MgO(barrier)/Fe(6 nm)/MgO(20 nm).

To carry out these measurements, we used on-chip devices to assure comparability and reproducibility [32]. These devices were prepared using conventional UV lithography. The fabrication process involved patterning the full stack and subsequently ion milling, controlling the milled thickness. An insulating SiO$_2$ layer with a thickness of 200 nm was grown by rf sputtering. In another lithography step, the heater was patterned on top of the insulating layer and evaporated using a Ti(10 nm)/Au(150 nm) stack. The dimensions of the active bar in the thermospin devices were 10×160 μm. An optical image of the devices used as well as a 3D sketch are shown in Fig. 13.

In our setup an electromagnet is used to apply an external magnetic field large enough to saturate the FM layer. A dc current is passed through the heater to generate a temperature gradient with a delay of 5 min to achieve temperature stability. From here, *I-V* curves are performed in order to obtain the samples and heater resistances for a more precise quantification of the SSE. The thermospin voltage (i.e., the raw voltage collected) is then collected by a nanovoltmeter while sweeping the magnetic field in the sample plane. Thermospin measurements were conducted on PdYBi, PtYBi, Pt control, and Fe reference samples. Typical data obtained for a PdYBi sample is displayed in Fig. 14(a). The left panel gives the voltage detected across the sample as a function of the applied magnetic field for different values of the heater
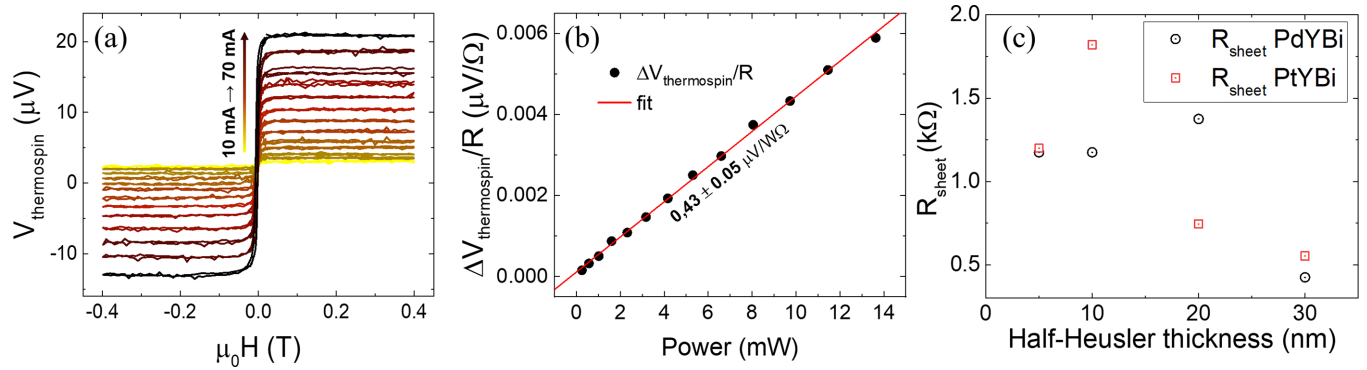
FIG. 14. (a) Raw data of the voltage detected as a function of magnetic field for different heater powers. (b) Amplitude of the voltage as a function of the heater power. Data given on (a) and (b) are obtained on the sapphire/PdYBi(20 nm)/MgO(1 ML)/Fe(6 nm)/MgO(20 nm) sample. (c) Sheet resistance as a function of half-Heusler film thickness for a set of samples with the stack sapphire/PdYBi(t)/MgO(20 nm) and similarly for PtYBi.

current. The detected voltage $V_{thermospin}$ at saturation increases linearly with heater power [Fig. 14(b)]. Its amplitude can be extracted by $\Delta V_{thermospin} = \frac{V^{H>0}_{thermospin} - V^{H<0}_{thermospin}}{2}$, where $H > 0$ and $H < 0$ are saturating magnetic fields at positive and negative values, respectively. The amplitude of the thermospin voltage is directly related to the SSE, but care must be taken since the ferromagnetic material adds a contribution coming from the anomalous Nernst effect (ANE). The ANE is generated according to the following relation: $\mathbf{E}_{ANE} \propto \nabla T \times \mathbf{M}$, where ∇T is along the z direction and M is along the applied magnetic field (along the y direction). Therefore the ANE voltage shares the same geometry as the SSE (since $\mathbf{E}_{ISHE} \propto \mathbf{J}_S \times \sigma$ and $\mathbf{J}_S // \nabla T$ and $\sigma // \mathbf{M}$) and is also proportional to the FM magnetization adding a supplementary detected voltage (along the x direction) that must be subtracted to isolate the voltage coming from the spin conversion in the half-Heusler, V_{SSE}.

The voltage reported in Fig. 14(a) thus contains a mixing of SSE and ANE contributions due to the measurement geometry. In order to solely extract the voltage generated by the SSE, a rectification must be done thanks to additional measurements conducted on a single Fe reference sample. The absence of strong SOC material in direct contact with the FM (in the reference sample) allows us to probe the ANE contribution alone and to perform the ANE correction of Fe on half-Heusler and Pt control samples afterward. Indeed, by considering shunting in parallel resistance mode, Ramos *et al.* [33] demonstrated that the ANE correction can be estimated according to the following equation:

$$\Delta V^{TI/Fe}_{ANE} = \frac{r}{1+r} \cdot \Delta V^{Fe}_{ANE} \quad \text{with} \quad r = \frac{R^{TI}_{sheet}}{R^{FM}_{sheet}}, \qquad (2)$$

where ΔV^{Fe}_{ANE} is the voltage amplitude detected across the sample for the Fe reference sample, R^{FM}_{sheet} and R^{TI}_{sheet} are the sheet resistances of the Fe and the half-Heusler (or HM) layers, respectively. It is then possible to subtract the ANE contribution to the thermospin voltage, ΔV^{Fe}_{ANE}, to get the overall S2C contribution, V_{SSE}. In this case, in order to ensure a good correction, the rectification is not performed directly on the voltage but on a normalized parameter given by $\frac{\Delta V_{thermospin}}{R_{sample} \times P}$, where R_{sample} is the sample resistance and P the

power injected in the heater [32]. This normalized quantity is plotted in Fig. 15 for the different samples prior and after the ANE correction. This correction is similar in all half-Heusler samples due to their large resistances. It is significantly different for the Pt control due to its lower resistance. It has been shown that Fe thin films present a negative ANE coefficient [34] when its thickness is in the range of the one in this study. We confirm this negative sign when comparing the Fe film to a YIG/Pt reference sample. The thermospin voltage detected is thus dominated by the ANE, as expected for a FM conductor, and its correction to obtain the SSE contribution leads to negative voltages in our systems. Moreover, the identical sign of V_{SSE} obtained for all samples confirms that both half-Heuslers have the same sign for S2C conversion than Pt.
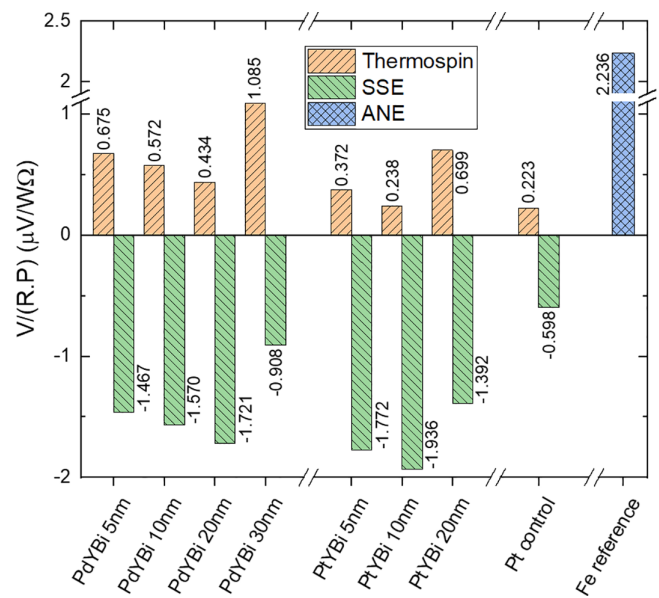

FIG. 15. Summary of the voltage normalized by the product between the power injected in the heater and the sample resistance for all half-Heusler thicknesses and Pt control sample. Orange columns are the raw voltages detected without ANE correction. The green columns are the SSE voltages (i.e., thermospin voltage after ANE correction).

The data given in Fig. 15 depict a larger SSE-generated voltage in PdYBi and PtYBi compared to the Pt control sample for all of the half-Heuslers. For TIs, since the carriers are localized in the surface, the voltage should keep the same value regardless of the thickness of the film. We cannot draw conclusions regarding this point, since we observe differences of up to 50% in the normalized SSE voltage ($\frac{\Delta V_{\text{SSE}}}{R_{\text{sample}} \times P}$) for our layers. The typical precision of thermospin measurements in these devices is much higher than the differences observed between samples; thus the differences could be attributed to disparities in the sample transport properties from one sample to another, including the possibility that they present additional bulk states at the Fermi energy. The most likely scenario is that we have a combination of bulk and surface conduction states. This is further confirmed by sheet resistance measurements shown in Fig. 14(c), where we observe a reduction for thicker samples, as expected for samples presenting bulk conducting states. The sheet resistance has been measured in a separate set of samples without the Fe layer by four-probe measurements in Hall bar devices. In a TI without any bulk conducting states, the R_{sheet} is constant for different TI thicknesses. We do not observe a divergence of R_{sheet} for lower thicknesses, indicating that it is likely there are also 2D states present in the conduction.

IV. CONCLUSIONS

We have grown epitaxial PdYBi and PtYBi thin films in the C1$_b$ half-Heusler structure in which they are predicted to potentially host a nontrivial topological state. Even if both compounds are very similar and crystallize along the (111) direction, some differences must be noted. Concerning the crystalline quality, the surface quality is higher in PdYBi with a lower roughness compared to PtYBi, although atomic disorder occurs in PdYBi, meanwhile PtYBi presents an excellent chemical ordering. However, two epitaxial variants were observed in PtYBi, leading to two domains turned by 180°. Strong similarities with the literature's band structure of both PtYBi and PdYBi allowed us to identify the manifestation of the nontrivial topology highlighted by the Γ_6 band located below the Fermi energy. Thermospin measurements reveal that the spin-to-charge interconversion in both PtYBi and PdYBi is significant and in all cases larger than a Pt prototype control sample. We observe some small variations in the spin conversion with the thickness of the half-Heusler films, and thus we think that bulk conducting states contribute together with surface conduction states to the observed voltage in thermospin measurements.

Even though further research is needed to fully understand the nature of the observed linear states and their potential for spin conversion in these materials, it is clear that our observations offer exciting opportunities for exploring topological properties in half-Heusler compounds and developing novel electronic and spintronic devices based on these materials.

[1] M. N. Baibich, J. M. Broto, A. Fert, F. Nguyen Van Dau, F. Petroff, P. Eitenne, G. Creuzet, A. Friederich, and J. Chazelas, Giant Magnetoresistance of (001)Fe/(001)Cr Magnetic Superlattices, Phys. Rev. Lett. **61**, 2472 (1988).

[2] G. Binasch, P. Grünberg, F. Saurenbach, and W. Zinn, Enhanced magnetoresistance in layered magnetic structures with antiferromagnetic interlayer exchange, Phys. Rev. B **39**, 4828 (1989).

[3] J. Slonczewski, Current-driven excitation of magnetic multilayers, J. Magn. Magn. Mater. **159**, L1 (1996).

[4] S. Bhatti, R. Sbiaa, A. Hirohata, H. Ohno, S. Fukami, and S. Piramanayagam, Spintronics based random access memory: A review, Mater. Today **20**, 530 (2017).

[5] B. Dieny, I. L. Prejbeanu, K. Garello, P. Gambardella, P. Freitas, R. Lehndorff, W. Raberg, U. Ebels, S. O. Demokritov, J. Akerman *et al.*, Opportunities and challenges for spintronics in the microelectronics industry, Nat. Electron. **3**, 446 (2020).

[6] A. Manchon, J. Železný, I. M. Miron, T. Jungwirth, J. Sinova, A. Thiaville, K. Garello, and P. Gambardella, Current-induced spin-orbit torques in ferromagnetic and antiferromagnetic systems, Rev. Mod. Phys. **91**, 035004 (2019).

[7] J. E. Hirsch, Spin Hall Effect, Phys. Rev. Lett. **83**, 1834 (1999).

[8] V. Edelstein, Spin polarization of conduction electrons induced by electric current in two-dimensional asymmetric electron systems, Solid State Commun. **73**, 233 (1990).

[9] L. Liu, O. J. Lee, T. J. Gudmundsen, D. C. Ralph, and R. A. Buhrman, Current-Induced Switching of Perpendicularly Magnetized Magnetic Layers using Spin Torque from the Spin Hall Effect, Phys. Rev. Lett. **109**, 096602 (2012).

[10] C. Pai, L. Liu, Y. Li, H. Tseng, D. Ralph, and R. Buhrman, Spin transfer torque devices utilizing the giant spin Hall effect of tungsten, Appl. Phys. Lett. **101**, 122404 (2012).

[11] L. Fu and C. L. Kane, Topological insulators with inversion symmetry, Phys. Rev. B **76**, 045302 (2007).

[12] J. Han, A. Richardella, S. A. Siddiqui, J. Finley, N. Samarth, and L. Liu, Room-Temperature Spin-Orbit Torque Switching Induced by a Topological Insulator, Phys. Rev. Lett. **119**, 077702 (2017).

[13] M. Z. Hasan and C. L. Kane, Colloquium: Topological insulators, Rev. Mod. Phys. **82**, 3045 (2010).

[14] Y. Xia, D. Qian, D. Hsieh, L. Wray, A. Pal, H. Lin, A. Bansil, D. Grauer, Y. Hor, R. Cava, and M. Hasan, Observation of a large-gap topological-insulator class with a single Dirac cone on the surface, Nat. Phys. **5**, 398 (2009).

[15] Y. Chen, J. Analytis, J. Chu, Z. Liu, S. Mo, X. Qi, H. Zhang, P. Lu, X. Dai, Z. Fang, S. Zhang, I. Fisher, Z. Hussain, and Z. Shen, Experimental realization of a three-dimensional topological insulator, Bi$_2$Te$_3$, Science **325**, 178 (2009).

[16] D. Hsieh, D. Qian, L. Wray, Y. Xia, Y. Hor, R. Cava, and M. Hasan, A topological Dirac insulator in a quantum spin Hall phase, Nature (London) **452**, 970 (2008).

[17] J. Sasaki, S. Namba, S. Takahashi, Y. Hirayama, and P. N. Hai, Highly efficient spin current source using BiSb topological insulator/NiO bilayers, Jpn. J. Appl. Phys. **62**, SC1005 (2023).

[18] J.-C. Rojas-Sánchez and A. Fert, Compared Efficiencies of Conversions between Charge and Spin Current by Spin-Orbit Interactions in Two- and Three-Dimensional Systems, Phys. Rev. Appl. **11**, 054049 (2019).

[19] S. Chadov, X. Qi, J. Kübler, G. Fecher, C. Felser, and S. Zhang, Tunable multifunctional topological insulators in ternary Heusler compounds, Nat. Mater. **9**, 541 (2010).

[20] B. Bernevig, T. Hughes, and S. Zhang, Quantum spin Hall effect and topological phase transition in HgTe quantum wells, Science **314**, 1757 (2006).

[21] C. Liu, Y. Lee, T. Kondo, E. D. Mun, M. Caudle, B. N. Harmon, S. L. Bud'Ko, P. C. Canfield, and A. Kaminski, Metallic surface electronic state in half-Heusler compounds RPtBi (R = Lu, Dy, Gd), Phys. Rev. B **83**, 205133 (2011).

[22] J. Logan, S. Patel, S. Harrington, C. Polley, B. Schultz, T. Balasubramanian, A. Janotti, A. Mikkelsen, and C. Palmstrøm, Observation of a topologically non-trivial surface state in half-Heusler PtLuSb (001) thin films, Nat. Commun. **7**, 11993 (2016).

[23] Z. Liu, L. Yang, S. Wu, C. Shekhar, J. Jiang, H. Yang, Y. Zhang, S. Mo, Z. Hussain, B. Yan, C. Felser, and Y. Chen, Observation of unusual topological surface states in half-Heusler compounds LnPtBi (Ln = Lu, Y), Nat. Commun. **7**, 12924 (2016).

[24] H. Lin, L. Wray, Y. Xia, S. Xu, S. Jia, R. Cava, A. Bansil, and M. Hasan, Half-Heusler ternary compounds as new multifunctional experimental platforms for topological quantum phenomena, Nat. Mater. **9**, 546 (2010).

[25] Y. Nakajima, R. Hu, K. Kirshenbaum, A. Hughes, P. Syers, X. Wang, K. Wang, R. Wang, S. R. Saha, D. Pratt, J. W. Lynn, and J. Paglione, Topological RPdBi half-Heusler semimetals: A new family of noncentrosymmetric magnetic superconductors, Sci. Adv. **1**, e1500242 (2015).

[26] Sanjeev, M. Singh, R. Kumar, S. Srivastava, and T. Kumar, *Ab-initio* study of topological phase tuning in half-Heusler YPdBi compound, Phys. B: Condens. Matter **640**, 414056 (2022).

[27] W. Al-Sawai, H. Lin, R. S. Markiewicz, L. A. Wray, Y. Xia, S.-Y. Xu, M. Z. Hasan, and A. Bansil, Topological electronic structure in half-Heusler topological insulators, Phys. Rev. B **82**, 125208 (2010).

[28] C. Guillemard, S. Petit-Watelot, T. Devolder, L. Pasquier, P. Boulet, S. Migot, J. Ghanbaja, F. Bertran, and S. Andrieu, Issues in growing Heusler compounds in thin films for spintronic applications, J. Appl. Phys. **128**, 241102 (2020).

[29] M. Hosen, G. Dhakal, K. Dimitri, H. Choi, F. Kabir, C. Sims, O. Pavlosiuk, P. Wiśniewski, T. Durakiewicz, J. Zhu, D. Kaczorowski, and M. Neupane, Observation of Dirac state in half-Heusler material YPtBi, Sci. Rep. **10**, 12343 (2020).

[30] K. Uchida, M. Ishida, T. Kikkawa, A. Kirihara, T. Murakami, and E. Saitoh, Longitudinal spin Seebeck effect: From fundamentals to applications, J. Phys.: Condens. Matter **26**, 343202 (2014).

[31] J. Zhang, J. P. Velev, X. Dang, and E. Y. Tsymbal, Band structure and spin texture of Bi_2Se_3 3D ferromagnetic metal interface, Phys. Rev. B **94**, 014435 (2016).

[32] A. Anadón, E. Martin, S. Homkar, B. Meunier, M. Vergés, H. Damas, J. Alegre, C. Lefevre, F. Roulland, C. Dubs, M. Lindner, L. Pasquier, O. Copie, K. Dumesnil, R. Ramos, D. Preziosi, S. Petit-Watelot, N. Viart, and J.-C. Rojas-Sánchez, Thermal Spin-Current Generation in the Multifunctional Ferrimagnet $Ga_{0.6}Fe_{1.4}O_3$, Phys. Rev. Appl. **18**, 054087 (2022).

[33] R. Ramos, T. Kikkawa, K. Uchida, H. Adachi, I. Lucas, M. Aguirre, P. Algarabel, L. Morellón, S. Maekawa, E. Saitoh, and M. Ibarra, Observation of the spin Seebeck effect in epitaxial Fe_3O_4 thin films, Appl. Phys. Lett. **102**, 072413 (2013).

[34] T. C. Chuang, P. L. Su, P. H. Wu, and S. Y. Huang, Enhancement of the anomalous Nernst effect in ferromagnetic thin films, Phys. Rev. B **96**, 174406 (2017).